AGU ADVANCING EARTH AND SPACE SCIENCE

Geophysical Research Letters

RESEARCH LETTER

10.1029/2020GL089632

Key Points:

- Australian continental margin is detected beneath Timor by passive seismic imaging with new broadband data along the Banda Arc
- Across arc structural variations in the crust reveal the collision of the Australian continent with the Banda forearc terrane
- The progressive structural changes along strike reflect different collisional stages as a result of oblique plate convergence

Supporting Information:

- Supporting Information S1

Correspondence to:

P. Zhang,
ping.zhang@anu.edu.au

Citation:

Zhang, P. & Miller, M. S. (2021). Seismic imaging of the subducted Australian continental margin beneath Timor and the Banda Arc collision zone. *Geophysical Research Letters*, *48*, e2020GL089632. https://doi.org/10.1029/2020GL089632

Received 11 JUL 2020
Accepted 24 NOV 2020

Seismic Imaging of the Subducted Australian Continental Margin Beneath Timor and the Banda Arc Collision Zone

Ping Zhang[1,2] and Meghan S. Miller[1]

[1]Research School of Earth Sciences, Australian National University, Canberra, NSW, Australia, [2]Deep Earth Imaging, Future Science Platform, CSIRO, Perth, WA, Australia

Abstract Detailed crustal and uppermost mantle structure is imaged for the first time utilizing ∼4 years of broadband seismic data newly collected in the Timor-Leste and Nusa Tenggara Timor region of Indonesia. We apply three techniques, ambient noise tomography, teleseismic *P* wave receiver function, and coda autocorrelation, to resolve a 3D Vs model and Moho structure. Our tomographic images show low-velocity anomalies (<30 km) beneath Timor related to underthrusted Gondwana sequence from the Australian plate, which are vertically offset by the high-velocity backstop of the Banda forearc terrane. The structure progressively changes along strike, reflecting different collisional stages developed as a result of the oblique convergence. At greater depth, we detect seismically fast lithospheric mantle (>30 km) and the arc-ward dipping Moho beneath Timor, both interpreted to be from the Australian plate. Our findings provide direct structural evidence of the Australian continental margin at lithospheric depths beneath the Banda Arc collisional zone.

Plain Language Summary The accretion of partial, or entire, volcanic arcs to a continental margin as they collide with a continent is one of the major processes in which new material is added to the crust over geological time. It also plays an important role in recycling crustal material back into the mantle via possible continental deep subduction. The Banda Arc–Australian continent collision currently taking place in SE Asia is one of the most classic examples of such process, yet its detailed deep structure that is critical to our understanding on how it evolves is still unclear due to the previous lack of dense data coverage. Resulting from a new seismic experiment consisting of 30 seismometers across the collisional zone and utilizing three complementing imaging techniques, we detect direct structural evidence of the underthrusted Australian passive margin at lithospheric depths with different components (continental crust, lithospheric mantle, and their boundary) beneath the Timor island.

1. Introduction

The active arc-continent collision in the Banda Arc is a result of convergence of the Indo-Australian plate with the Eurasian plate in southeast Asia. It captures the tectonic transition from subduction of the Cretaceous to Jurassic age Indian Ocean lithosphere along the Sunda Arc in the west to the recent collision of the Australian continental margin with the forearc complex attached to an active volcanic arc in the east (e.g., Harris, 2011; Keep & Haig, 2010, Figure 1). Here, the volcanic arc, referred to as the inner arc, spans from the island of Flores with active volcanism westward into an extinct sector of volcanoes nearby islands of Alor and Wetar (Figure 1). This cessation of volcanism (∼3 Ma ago) has been inferred to relate to subduction of continental materials (Harris, 2011). Most volcanic rocks in western Flores consist of primitive basalts typical of a volcanic arc built on oceanic lithosphere, while the arc volcanism in eastern Flores bears continental isotopic signatures, suggesting the involvement of subducted continental material in magma genesis (Elburg et al., 2004, 2005; Hilton & Craig, 1989; Hilton et al., 1992; Figure 1). The outer arc system marks the collisional front that includes the island of Timor west along to the islands of Rote and Savu, which is the orogenic product of that collision (Figure 1). Sumba, which strikes WNW in contrast to the other outer arc islands, is situated at the junction of the Sunda Arc subduction system and the Banda Arc collision system, but its geology shows very little involvement with the tectonics of either (e.g., Chamalaun et al., 1982). The Savu Sea is an elongate forearc basin that lies in between these two bifurcated arcs in the convergent system. Investigation into the complex tectonic evolution of this young arc-continent collision is important in understanding many fundamental processes, such as formation of mountain belts, growth

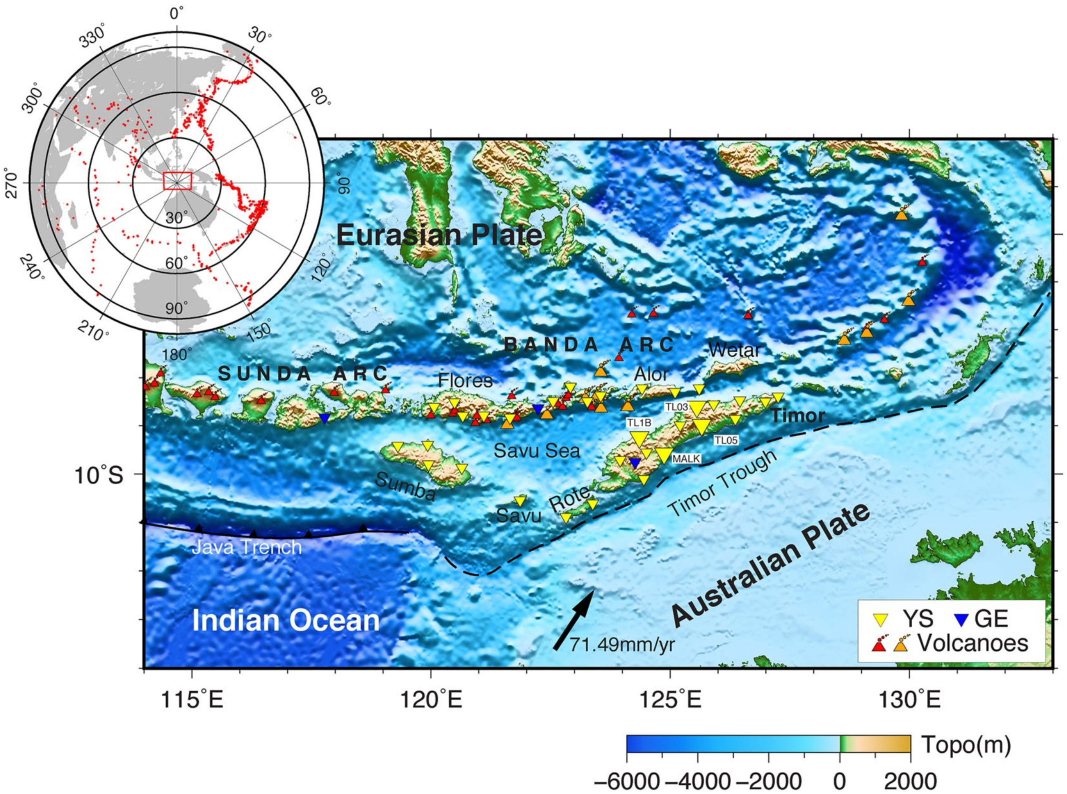

Figure 1. Tectonic and topographic map of the Banda Arc and seismic stations deployed in the study region. Inverted triangles mark the temporary deployments of the YS array (yellow) and the three permanent stations from the GE network (blue). Red triangles with bubbles represent the active arc volcanoes (Siebert & Simkin, 2002). Orange triangles with bubbles indicate volcanoes with anomalously low values of $^3He/^4He$ ratios from Hilton and Craig (1989) and Hilton et al. (1992), which have been attributed to the involvement of the continental margin. The black solid line with sided triangles represents the Java Trench and the black dashed line marks the Timor Trough (modified after Hall, 2017; Pownall et al., 2013). The black arrow indicates the plate motion at 123°E and −13°S calculated from the NUVEL-1A model (DeMets et al., 1994). Major plates, tectonic units, and islands referred to in text are labeled. Stations shown in Figure 3 are labeled with white backgrounds and have larger symbol size. Inset shows global event distributions used for receiver function and autocorrelation analyses, where the study region is outlined by a red rectangular box.

of continental crust, and recycling of material into the deep mantle, which have shaped Earth's long-term evolution.

Published seismic tomography images have advanced our understanding of the arc-continent collisional processes in the Banda Arc region. Most early studies focused on large-scale tectonic evolution by imaging the slab morphology along the entire Sunda–Banda Arc system with global datasets (e.g., Hafkenscheid et al., 2001; Spakman & Hall, 2010; Widiyantoro & van der Hilst, 1996, 1997; Widiyantoro et al., 2011). Some more regionally focused studies addressed possible hypotheses that dominate the collisional evolution in Banda such as deep subduction of the Australian continent, the presence of ancient continental terranes and slab tears, but they only resolve mantle structure at depth greater than ~60–100 km (Fichtner et al., 2010; Harris et al., 2020; Zenonos et al, 2019, 2020). Most recently, Supendi et al. (2020) developed a new *P* wave velocity (Vp) model at depths above 120 km using local earthquakes for which they propose that a seismically fast forearc sliver of continental origin is underthrusted beneath Flores and accounts for the arc volcanism contamination. Porritt et al. (2016) produced a shear wave velocity (Vs) tomography model of the upper 50 km beneath the region based on classic two-step ambient noise tomography with ~18-month duration data set. Their results depict a consistent downward extension of the geologically inferred stratigraphy of Banda Terrane and Gondwana sequence at crustal scale in a broad view. However, the velocity anomalies in their images appear interlayered vertically, which may reflect the nonuniqueness of the

10.1029/2020GL089632

inversion of a relatively small amount of dispersion data or lack of spatial coherence in the two-step method of ambient noise tomography. Therefore, a comprehensive high-resolution seismic structure at crustal scale targeting this key tectonic region is still required in order to examine the variable hypotheses proposed based on other disciplines and/or mantle-scale seismic images. Such model will be also important to refine the deep mantle images, collectively serving as seismic reference that helps to address deep dynamics at the Banda Arc collisional zone.

In this study, we apply three imaging techniques to ∼4 years' worth of data from a new temporary seismic experiment deployed in the Banda Arc region along with all available permanent stations to reveal detailed crustal-scale structures unable to be resolved in previous studies and provide insight into the collisional tectonics. First, we present a new 3D Vs model for the crust and uppermost mantle using a novel direct surface wave inversion algorithm with ambient noise data (Fang et al., 2015). As crustal thickness is typically poorly constrained by surface wave data alone, we combine these results with complementary imaging techniques: teleseismic *P* wave receiver function (i.e., conversions) and coda autocorrelation (i.e., reflections). Both methods are particularly sensitive to discontinuity structures, which provide independent constraints on the Moho and thus aid our interpretation of the crustal and mantle structures previously unresolved with passive seismic imaging.

2. Data and Methods

The Banda Arc passive seismic experiment consists of 30 broadband seismometers (YS array; Miller, 2014) deployed in the Timor-Leste and Nusa Tenggara Timur (NTT) region of the eastern Indonesia (Miller et al., 2016, Figure 1). Eight instruments were deployed in Timor-Leste from March 2014 to the end of 2018 and the others in the NTT region were deployed from October 2014 until August 2019. In addition, we include continuous data from three permanent stations of the GE network (GEOFON Data Centre, 1993) located in our study region (Figure 1). In the following, we describe the three methods applied to these data: ambient noise tomography model that resolves the Vs in the crust and uppermost mantle; teleseismic *P* wave receiver function; and teleseismic coda autocorrelation analyses used to constrain Moho-generated conversions and reflections, respectively.

2.1. Ambient Noise Tomography

We measure Rayleigh wave phase velocity dispersions (6–37 s) using approximately 4 years of continuous records (March 2014 to December 2018) following the procedures described by Bensen et al. (2007) and Porritt et al. (2016). First, we process the continuous daily vertical-component seismograms by removing mean, linear trends, and instrument responses. They are also tapered and down-sampled to 1 Hz from 50 sps. Next, we apply running-average time domain normalization and spectral whitening to minimize the effects of large earthquakes. Seismograms from all station pairs are cross-correlated and stacked over the entire time period of the deployment (e.g., Figure S1). We then measure interstation Rayleigh wave phase velocity dispersions between periods of 6 s and 37 s from symmetric cross-correlations (i.e., an average of positive and negative correlation lag) with the automated Frequency–Time Analysis (e.g., Bensen et al., 2007). The path-based measurements are quality controlled with a minimum signal-to-noise ratio of 4 and a minimum interstation path length of 1.5 wavelengths as a far-field criterion (e.g., Luo et al., 2015). Dispersion curves of all station pairs and number of measurements at each period are shown in Figure S2. Raypath coverage at different periods are presented in Figure S3.

Following Fang et al. (2015), we perform a 3D surface wave direct inversion to resolve the shear wave velocities in the crust and uppermost mantle. The new algorithm utilizes the fast-marching ray tracing method to calculate, at each period, synthetic travel times and raypaths between sources and receivers and subsequent directly inverts all data to a 3D Vs model. Unlike the traditional two-step method, an intermediate 2D velocity map is no longer required, and the great-circle propagation assumption is avoided by incorporating ray tracing in the new algorithm. Here, we use the AK135 1D velocity model (Kennett et al., 1995) as the initial model and the grids are set as 0.25° by 0.25° in the horizontal direction and 5 km in the vertical direction. We only invert for the upper 70 km. Vp and density are correspondingly calculated using empirical

10.1029/2020GL089632

relationships by Brocher (2005). Upon iteration, the raypaths and the data sensitivity matrix are updated based on the newly obtained model. After a series of trial tests, the weight parameter that balances data fitting and smoothing regularization term is set as 5 and the damping parameter that controls the amplitude of the inverted parameter in the LSQR solver is set as 0.1. Figure S4 presents checkerboard resolution tests, where similar parameter settings as used in real-data inversion were used with checker size of 0.75° by 0.75°. These tests show that the Vs model in upper 50 km can be robustly resolved in regions where data coverage is dense with lateral resolution of ∼60–80 km, although varying degrees of smearing are observed. More details about the method and parameter settings are described in Fang et al. (2015).

2.2. *P* Wave Receiver Functions

We analyze a total of 1,268 events with magnitude of >5.5 and epicentral distances between 30° and 95°, occurring from March 2014 to August 2019 based on the USGS NEIC global catalog (inset map in Figure 1). Over 50% of these events are clustered in the 70°–180° backazimuth range, 27% are in a range of 0°–50° and the rest fall within a range of 180° and larger. Preprocessing includes removing the linear trend and the mean, then applying a cosine taper with width of 0.315 s to each end of data. The original three component seismograms are rotated into *R*–*T*–*Z* coordinate system. We compute *P* wave receiver functions using an iterative deconvolution approach in the time domain (Ligorria & Ammon, 1999) with a Gaussian width of 2.5 from Herrmann (2013). These receiver functions are manually reviewed and selected using the Funclab toolbox (Eagar & Fouch, 2012; Porritt & Miller, 2018). In this study, we focus on four representative stations for further analysis (see station locations in Figures 1 and 2). Detailed discussion is addressed in Section 4.2. For each station, we identify both Moho-generated Ps conversions and surface-reflected PpPs multiples by integrating thorough analyses on the secondary PpSs + PsPs multiples converted from the Moho, azimuthal varied plots, and theoretical calculation on the delay time of all considered phases based on station-specific 1D models interpolated from ambient noise tomography (Figures 3 and S5–S10).

2.3. Coda Wave Autocorrelation

The autocorrelations of teleseismic *P* wave coda correspond to reflections below a single station (Claerbout, 1968). With the same data set used for receiver function analyses, we apply the autocorrelation processing steps outlined by Phạm and Tkalčić (2017) to vertical-component waveforms. First, a spectral whitening with an empirical width of 0.1 Hz is applied to normalize the complex spectrum of the original waveforms. This processing helps to address the influence of the source and path effects by homogenizing the contribution of frequency components in an appropriate band. We then compute the autocorrelation of the whitened waveform in the frequency domain and only retain the positive time lags of the symmetric autocorrelograms after transferring to the time domain. A cosine taper with 0.5 s width is applied to suppress the characteristic peak at zero-time. Also, a zero-phase band-pass filter of 0.25–1.0 Hz is used to highlight the target signal by removing very long period signals and spurious high-frequency noise induced by the spectral whitening. Next, all traces are normalized and stacked with both linear and phase-weighted stacking method (Figure S11). To highlight the coherent signals that address first-order discontinuity, we also calculate correlation coefficient between each trace and the linear stack of station in a selected window and remove those autocorrelograms with small coefficient. In Figure 3, we only show those traces with coefficient larger than 0.5 and the corresponding linear stack, in which *P* wave reflections from the Moho (PpPp) stand out on the waveforms. In practice, we identify the Moho reflections by considering their coherent and robust presence on different subset of autocorrelograms and variable stacks as well as their consistency with the Moho conversions (Figures 3 and S6–S11).

3. Results

3.1. Tomographic Images

The 3D Vs model of the crust and uppermost mantle derived by ambient noise tomography is shown as horizontal slices at different depths and vertical cross-sections along the orogenic strike in Figure 2. The primary

10.1029/2020GL089632

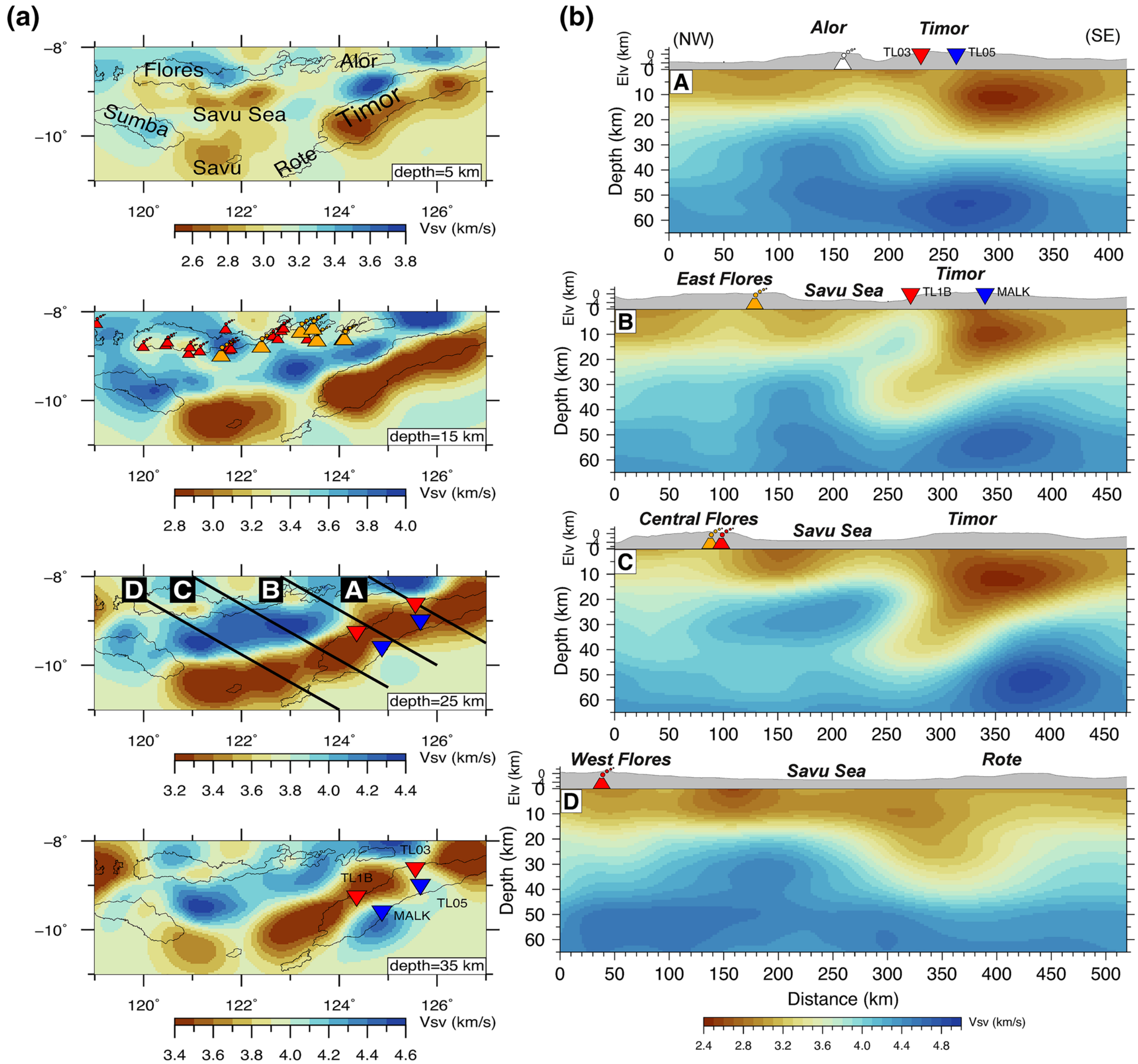

Figure 2. 3D Vs model in the crust and uppermost mantle derived from ambient noise tomography. (a) Map views of the Vs model at depths of 5, 15, 25, and 35 km as indicated in the lower right corner of each panel. Major islands and the Savu Sea are labeled in the top panel; volcanoes (red and orange triangles with bubbles as in Figure 1) are shown in the second panel; locations of the vertical profiles are shown in the third panel; and station locations and names used for teleseismic analysis (red and blue inverted triangles) are marked in the third and bottom panels. (b) Northwest-to-southeast orientated vertical cross-sections through the model with topography and bathymetry on the top, showing the progressive structural variations along the orogenic strike. The color coded triangles with smoke bubbles along different profiles represent the arc extinction sector close to Alor (white), volcanism contaminated arc sector in East Flores (orange), transitional volcanism sector in the central Flores (orange and red), and the typical subduction-related arc sector in West Flores (red). Red and blue inverted triangles are the same stations as in (a).

velocity anomalies strike in a southeast-to-northwest direction, roughly parallel to the Timor Trough and the coastlines of Timor and Rote. In Figure 2a, the structure beneath the inner arc islands of Flores and Alor as well as the forearc basin of Savu Sea is largely characterized by relatively fast velocities in the upper 50 km. In contrast, the structure beneath the outer arcs, across the islands of Savu, Rote, and Timor, generally has low-velocity anomalies at the same depth range. At 35 km depth, we observe a prominent high-velocity anomaly in a northeast-southwest orientation beneath Timor that is surrounded by slow velocities.

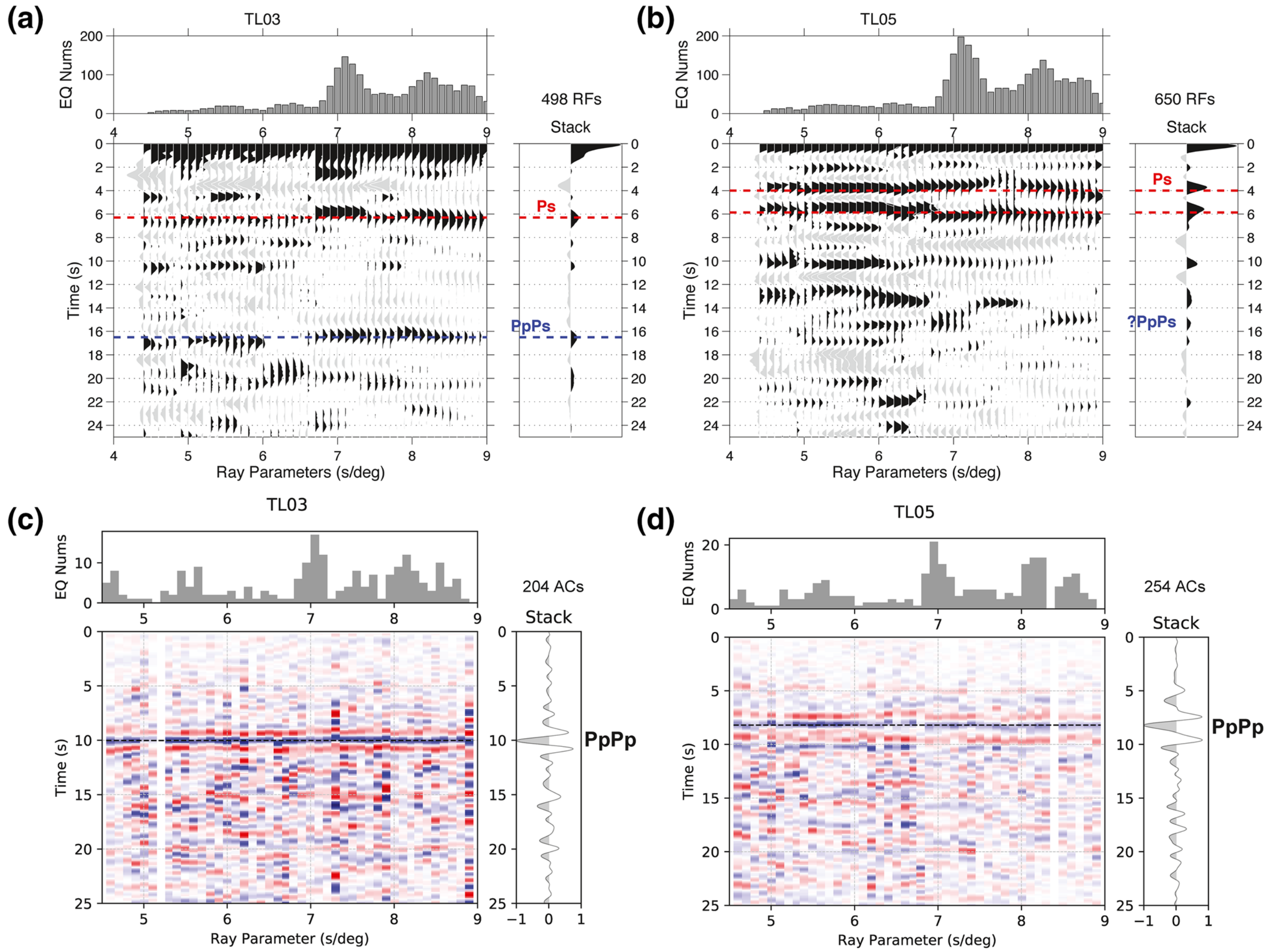

Figure 3. *P* wave receiver functions (RFs) and autocorrelograms (ACs) for stations TL03 and TL05 located on the island of Timor (see Figure 2 for locations). RFs (a and b) are ranged and binned by ray parameter (bin size are 0.1 s/deg), with two-bin smoothing on both sides for each binned trace. Dashed lines mark delay times of the interpreted converted phases (i.e., Ps is in red and PpPs is in blue). ACs (c and d) are ranged and binned by ray parameter with the same bin size. The dominant negative signals (blue in the image and gray in the stack) are the interpreted PpPp reflections. In each figure, the top panel is a histogram of numbers of traces in each bin. The right-side column is a linear stack of all binned traces and the total number is denoted on the top. Note that the total RF numbers indicated in the histogram are larger than real measurement numbers due to the smoothing. All interpreted phases including Ps conversions, surface-reflected PpPs multiples, and *P* wave reflections (i.e., PpPp) are labeled.

This feature extends from central Timor at 30 km depth where it spans most of region beneath the island of Timor at depth greater than 40 km. The slow velocities charactering Timor in the upper 30 km also migrates northwestward with increasing depth and mainly concentrate in the forearc region beneath the southeast Savu Sea at depths greater than 40 km. The observed pattern of both high-velocity and low-velocity anomalies beneath Timor suggests the presence of a discontinuity at this depth range (~30–45 km), separating the slow materials above and the fast materials below, and it dips toward the inner arc (northwestward).

These features are more clearly presented in vertical Profiles A–D through the model in Figure 2b. First, along the orogenic strike of Timor from northeast (Profile A) to southwest (Profile D), we observe a progressive change in the shape of both high velocities beneath Flores and Savu Sea in the northwest (at distance <200 km along the profile) and low velocities beneath Timor and Rote in the southeast (at distance >250 km along the profile). In Profile A, the contact of the two anomalies is sharp but then becomes progressively less sharp to the southwest as shown in Profiles B–D. Second, the imaged low velocities beneath Timor at 250 km and greater along the Profiles A–C appear to dip northward with increasing depth and reach to the depth of 30–40 km in the northwestern end. Below these anomalies, we observe high-velocity

10.1029/2020GL089632

structural features at deeper depths (>30 km). Along Profiles A–C, the top of this fast structure is present at ~30 km depth in the southeast and migrates down to 40 km in the northwest, suggesting a similar arc-ward dipping pattern as that for the overlying slow materials. The northwestward dipping feature revealed in this depth range is robust as we have sufficient and high-quality measurements at period of ~20–30 s that is able to constrain the Vs structure at these depths (Figures S2–S4).

3.2. Moho-Generated Conversions and Reflections

We present receiver function and autocorrelation results for two sets of representative stations located on the island of Timor (Figures 3 and S6–S11). Two stations are along the tomographic Profile A and the other two are along Profile B, with stations TL03 and TL1B on the northwestern side of Timor and stations TL05 and MALK on the southeastern side of the island (see Figures 1 and 2 for station locations).

In general, there are positive signals with large amplitude in two time-windows (~4–6 s and ~14–16 s) in the receiver function waveforms (Figures 3a, 3b and S6–S10). We identify these as Moho-generated Ps conversions and surface-reflected PpPs multiples, respectively. For station TL03, the positive Ps signal at ~6 s and PpPs signal at ~16 s from the Moho are prominent in receiver functions (Figures 3a and S7). We can continuously track both phases in individual traces across all waveforms and easily identify them in the station stack (Figures 3a and S6). In contrast, receiver function waveforms for station TL05 are more complex (Figures 3b and S8). We observe two positive signals at ~4 s and ~6 s that can be considered as potential Moho-generated Ps conversions (Figures 3b and S8). Near ~15 s, where the PpPs multiples are expected for a discontinuity at ~35 km depth beneath the station, positive signals are observable; however, their presence is intermittent on the ray parameter sorted waveforms and is weak and scattered in the receiver function stack (Figures 3b and S8). Both the Ps (~6 s) and PpPs (~16 s) signals are visible in the TL1B station waveforms but the amplitudes are very small (Figures S6a and S9). For station MALK, there are complex signals on the raw waveforms but the conversions from the Moho (Ps at ~4 s and PpPs at ~14 s) are still distinguishable considering their continuity across all waveforms and the large amplitude in the stack (Figures S6b and S10).

Autocorrelation results for these four stations are presented in Figures 3c and 3d and S10. For station TL03, a negative polarized peak at ~10 s has a large amplitude in the individual autocorrelograms and in the stacks (Figures 3c and S11a). We interpret this signal as the *P* wave reflections from the Moho (i.e., PpPp). A prominent high-amplitude negative signal is also seen near 8 s in the autocorrelograms of station TL05, which is identified as the PpPp reflections (Figures 3d and S11b). In this case, where the receiver function waveforms are complicated (Figure 3b), the reflections revealed through the autocorrelation technique provide important complementary information. Results of TL1B show a sharp negative PpPp signal at ~11 s in the stack (Figure S11c). But we cannot observe a clear signal in the autocorrelograms nor the stack in the time window for the predicted Moho reflection for station MALK (Figure S11d). We address this issue with more detail in Section 4.2.

4. Discussions and Conclusions

4.1. Comparisons With Previous Tomographic Studies

There is general agreement with the ambient noise tomography model that used only 18 months of data and the two-step method (Porritt et al., 2016). Our model is an improvement over this initial model with the application of the novel 3D direct inversion algorithm and the use of ~30 additional months of data. In particular, the direct inversion algorithm avoids the great-circle propagation assumption by incorporating ray tracing and thus is an improvement from the two-step method when dealing with regions of strong structural heterogeneity (e.g., Fang et al., 2015; Li et al., 2016). The new images illustrate greater spatial (vertical and horizontal) structural coherence benefit from direct smoothing regularization on a three-dimensional model (Fang et al., 2015). The overall pattern in our Vs model is also comparable to the crustal structural heterogeneity revealed by the Vp model from recent local earthquake tomography (Supendi et al., 2020), but with reasonable differences due to the inherently different methodology and data sensitivities. The dissimilarities in structural features shown in the Vp and Vs models might also indicate anomalous Vp/Vs ratio structures that are correlated with possible partial melting or lithologic changes in the study region.

4.2. Receiver Function and Autocorrelation Joint Interpretation

The autocorrelograms in this study provide important complementary constraints on the Moho structure in comparison to using receiver function data alone (Figure 3), especially considering the highly heterogeneous structure. However, we also identify challenges in interpreting the results and applying the autocorrelation ubiquitously (e.g., Figures 3, S6 and S11). Moho-generated phases considered in this study (Ps, PpPs, and PpPp) have different lateral sampling, frequency content, and structural sensitivities. Conversions are primarily sensitive to changes in the Vs structure and depend weakly on the crustal Vp structure, whereas high-frequency reflections (autocorrelation traces) provide high resolution of crustal Vp reflectors (e.g., sharp Moho). Reverberations from shallow low-velocity layers (e.g., sediment or intracrustal anomaly) potentially interfere with Ps conversions but converted multiples (i.e., PpPs and PsPs + PpSs) and reflection phases (e.g., PpPp) can provide more robust images in these settings (e.g., Phạm & Tkalčić, 2017, 2018; Zhang et al., 2019). The influence of the source and path effects and simultaneous arrivals of multiple orders of reverberations have been a fundamental challenge in interpreting the autocorrelograms (e.g., Phạm & Tkalčić, 2017). However, the focus of this study is on first-order features, such as the Moho, that can be identified to aid our interpretation on tomographic images, rather than an exhausting analysis of the potential structural complexity bared in our data set. With these factors in consideration, we carefully select station pairs with high-quality measurements and only interpret the coherent Moho signals for two station pairs, that are also present in the ambient noise tomographic images.

Both Moho-generated conversions (Ps and PpPs) and reflections (PpPp) show relatively late arrivals for station TL03 at the northwest side of Timor, while all phases exhibit earlier arrivals for station TL05 at the southeast side of Timor (Figure 3). One-dimensional Vs models from ambient noise tomography for these two stations show that crustal materials beneath station TL03 are overall higher than that beneath station TL05 (Figure S5). Later arrivals of conversions for station TL03 require either a deeper Moho or a larger Vp/Vs ratio. The time differences in *P* wave reflections, which are independent of Vs, suggest either a deeper Moho depth or slower crustal Vp structure beneath station TL03. In this case, the velocity structure variations are not able to explain the observed time difference of all three phases between these two stations. Therefore, we conclude that the Moho beneath station TL03 located at the downdip direction is deeper than that for station TL05 at the updip direction, which indicates the presence of an arc-ward dipping Moho discontinuity at depth range of 30–40 km. Another station pair, TL1B, which is on the northern side of Timor, and MALK, which is on the southern side of Timor, along the tomographic Profile B also shows similar receiver function results (Figure S6) where the downdip station has a deeper Moho. This teleseismic-based observation well collaborates with the presence of an arc-ward dipping boundary indicated by ambient noise tomography in Figure 2. Thus, we conclude that it is an arc-ward dipping Moho discontinuity beneath the Timor is mapped with three independent but complement analyses.

4.3. Tectonic Implications

From the tomographic images (Figure 2), we interpret the dominant velocity variations across the Banda Arc to be structures resulting from the collision between the Banda Terrane and the incoming Australian lithosphere, but these 3D images are the first to infer the crustal and upper mantle structure of the entire collisional zone at high resolution. The wedge-shaped northward dipping slow materials beneath the outer arc sectors (i.e., Timor, Rote, and Savu, Figure 2) are interpreted to be related to the duplexed and underthrusted sedimentary and continental crustal materials from the Australian passive margin (Harris, 2011; Keep & Haig, 2010; Tate et al., 2015, 2017). These rocks are likely associated with the Gondwana sequence that represents the pre-breakup sedimentary cover and the overlying Australian Passive Margin sequence (Harris, 2011; Keep & Haig, 2010). The collective thickness of these stratigraphic units is documented to be up to ~10–15 km in the southern side of Timor, including Timor Trough (Petkovic et al., 2000; Shulgin et al., 2009) as well as the analogous Exmouth Plateau in Western Australia (Keep & Haig, 2010). Geological and geophysical studies also confirm the crustal shortening and active duplexing of the Australian strata and thrust nappes in Timor (e.g., Harris, 2011; Keep & Haig, 2010; Tate et al., 2015, 2017). In contrast, the relatively high-velocity structure beneath the inner arc and forearc basin (as shown in Figure 2) is interpreted as a backstop of the Banda Terrane. This terrane, composed of an assemblage of medium grade metamorphic rocks with overlying forearc basin deposits (Harris, 2006), has been accreted to the leading edge of the Australian plate in part but is likely still attached to the volcanic arc (Harris, 2006, 2011). In our images, this accreted terrane is mapped with faster seismic velocities in comparison to continental crustal velocities, similar to findings in other subduction and collision zones where current or future terrane accretion is involved (e.g., Tetreault & Buiter, 2014).

Across the island of Timor, geological mapping has documented that the forearc terrane structurally overlies the Gondwana sequence based on surface outcrops (Harris, 2011; Tate et al., 2015, 2017). Our tomographic images of the shallow crust (<30 km) correlate with these results. We observe the southeastward extent of high-velocity anomalies (i.e., upper plate) from Savu Sea to the northwestern edge of Timor and the northwestward dipping of those low-velocity anomalies (i.e., lower plate) beneath Timor (e.g., Profile B in Figure 2b). The strongest velocity contrast between these two structures, which we interpret as the collisional boundary of these two units, is along the northwest coastlines of Timor in the upper 30 km (Figure 2). These two velocity structures can be traced to deeper depths and the inferred collisional boundary migrates from northwestern Timor (<30 km) to southeastern part of Savu Sea to ∼ 30–40 km depth (Figure 2). This observation suggests that the Australian continental material is below the Savu Sea at these depths.

Therefore, we interpret the lateral velocity variations along orogenic strike shown by the cross-sections in Figure 2b to be the result of different collisional stages of the slightly oblique convergence of the Australian passive margin with Banda Arc (DeMets et al., 1994; as shown in Figure 1). Compared to other profiles, the relatively narrow forearc terrane is imaged in Profile A (Figure 2b), consistent with the inference that much of the forearc rocks has been accreted to the underthrusted Australian passive margin (e.g., Harris, 2011; Tate et al., 2015, 2017). In Profile A, the collisional boundary between the seismically fast forearc terrane and slow velocity Gondwana duplex is steep and the structural contact is sharp, which might reflect the strong coupling of these two terranes. Profile A cross the arc extinction sector (Alor) and Profile B cross the volcanism contaminated inner arc sector in East Flores, both of which suggest the involvement of continental materials at deep depths (Elburg et al., 2004, 2005; Hilton & Craig, 1989; Hilton et al., 1992). To the southwest, in Profiles C and D, the structural contact appears as a less sharp feature between the inferred arc and forearc rocks (high-velocity) and inferred Australian continental (low-velocity) materials. In particular, the structure in Profile D across the typical subduction-related arc sector of western Flores and Rote is significantly different than the other profiles crossing Timor. Here, the velocity contrast across the inner and outer arcs becomes less sharp and the extent pattern of the slow wedge beneath outer arc is also different from other profiles where the slow materials are dragged down to deep depths toward the inner arc. These observations support our inference that the collision is more mature at the northeastern edge of the study region (Profile A and its vicinity) but it is still in an initial stage in the southeast (Profile D and its vicinity), which is also supported by geological and geochemical studies (e.g., Harris, 2011).

In the tomographic images, we identify the observed high-velocity anomalies at depths greater than 30 km beneath Timor (Figure 2) as the lithospheric mantle material from the passive margin of Australian continent. Given that the inherent structure of the precollisional rifted Australian passive margin is highly heterogeneous (e.g., Harris, 2011; Keep & Haig, 2010; Spakman & Hall, 2010), this seismically fast lithospheric mantle imaged beneath Timor is probably composed of fragments of oceanic, continental, and volcanic compositions. The arc-ward dipping Moho of the underthrusted Australian plate beneath Timor, separating the slow continental crust above and the fast lithospheric mantle below, is coherently observed with all three imaging methods: receiver functions, autocorrelations, and ambient noise tomography. These findings consistently support the presence of the downgoing Australian passive margin at crust-to-mantle boundary and uppermost mantle depth across the Banda Arc collision zone.

Deep subduction of Australian continent in the Banda Arc region has been proposed to play an important role in the tectonic evolution of this young arc-continent collision. Previous earthquake tomography studies imaged broad seismic high-velocity structural features at deep depth beneath Banda Sea (>200 km, Fichtner et al., 2010) and Flores Island (>100 km, Harris et al., 2020) and associated them with the subducting Australian continental lithosphere. New structural geology-based mapping work in Timor-Leste and West Timor, respectively, also suggests that ∼210 km of Australian continental lithosphere has been subducted below the Banda forearc (Tate et al., 2015, 2017). Arc volcanism cessation in Alor, Wetar and contamination in eastern Flores support the involvement of a significant amount of continental materials at deep depths along the inner arc (Elburg et al., 2004, 2005; Hilton & Craig, 1989; Hilton et al., 1992). This work bridges the range of depths (from near to upper mantle depths) studied in these previous works by focusing on upper lithospheric scale structures inferred from our passive source imaging. We conclude from our complementary seismic imaging results that the arc-ward dipping slow velocities in the crust, the variable Moho structure, and the high-velocity lithospheric mantle imaged beneath Timor collectively indicate the presence of the underthrusted Australian passive margin in front of the Timor Trough.

Data Availability Statement

The data of YS array used in this study are archived at the IRIS Data Management Center and the Australian Passive Seismic Server (https://doi.org/10.7914/SN/YS_2014). The continuous data from permanent stations of GE network are available at the IRISDMC (https://doi.org/10.14470/TR560404). Our final model that supports the conclusion is available at the IRIS EMC-EarthModels repository at https://doi.org/10.17611/dp/emc.2020.bandaantcvs.1.

Acknowledgments
This research was supported by NSF-Tectonics/Geophysics/Global Venture fund grant EAR-1250214. P.Z. was supported by the CSIRO Deep Imaging Future Science Platform PhD scholarship. We acknowledge Dr Robert W. Porritt for providing the code for cross-correlation calculation and dispersion measurement, Dr Hongjian Fang for providing the direction inversion code (https://github.com/HongjianFang/DSurfTomo), and Dr Thanh-Son Pham for providing the code to compute the autocorrelograms. Figures were made with Generic Mapping Tools (http://gmt.soest.hawaii.edu), MATLAB (https://www.mathworks.com), and Python software (https://www.python.org). We thank Brian L.N. Kennett for his extensive discussions and comments in the process of producing the manuscript and improving its quality. We are grateful for the review by Dr Mehdi Qashqai at CSIRO that helps to improve the initial version of the manuscript. We appreciate the constructive criticism and suggestions from the editor, Jeroen Ritsema, and two reviewers Douwe van Hinsbergen and Luca De Siena, which have greatly improved the manuscript.

References

Bensen, G. D., Ritzwoller, M. H., Barmin, M. P., Levshin, A. L., Lin, F., Moschetti, M. P., & Yang, Y. (2007). Processing seismic ambient noise data to obtain reliable broad-band surface wave dispersion measurements. *Geophysical Journal International*, *169*(3), 1239–1260.

Brocher, T. M. (2005). Empirical relations between elastic wavespeeds and density in the Earth's crust. *Bulletin of the Seismological Society of America*, *95*(6), 2081–2092.

Chamalaun, F. H., Grady, A. E., Von der Borch, C. C., & Hartono, H. M. S. (1982). Banda arc tectonics: The significance of the Sumba Island. In J. S. Watkins & C. L. Drake (Eds.), *Studies in continental margin geology* (pp. 361–372). American Association of Petroleum Geologists.

Claerbout, J. (1968). Synthesis of a layered medium from its acoustic transmission response. *Geophysics*, *33*(2), 264–269. https://doi.org/10.1190/1.1439927

DeMets, C., Gordon, R. G., Argus, D. F., & Stein, S. (1994). Effect of recent revisions to the geomagnetic reversal time scale on estimates of current plate motions. *Geophysical Research Letters*, *21*(20), 2191–2194.

Eagar, K. C., & Fouch, M. J. (2012). FuncLab: A MATLAB interactive toolbox for handling receiver function datasets. *Seismological Research Letters*, *83*(3), 596–603.

Elburg, M. A., Van Bergen, M. J., & Foden, J. D. (2004). Subducted upper and lower continental crust contributes to magmatism in the collision sector of the Sunda–Banda arc, Indonesia. *Geology*, *32*(1), 41–44.

Elburg, M. A., Foden, J. D, van Bergen, M. J, & Zulkarnain, I. (2005). Australia and Indonesia in collision: Geochemical sources of magmatism. *Journal of Volcanology and Geothermal Research*, *140*, 25–47. https://doi.org/10.1016/j.jvolgeores.2004.07.014

Fang, H., Yao, H., Zhang, H., Huang, Y. C., & van der Hilst, R. D. (2015). Direct inversion of surface wave dispersion for three-dimensional shallow crustal structure based on ray tracing: Methodology and application. *Geophysical Journal International*, *201*(3), 1251–1263.

Fichtner, A., De Wit, M., & van Bergen, M. (2010). Subduction of continental lithosphere in the Banda Sea region: Combining evidence from full waveform tomography and isotope ratios. *Earth and Planetary Science Letters*, *297*(3–4), 405–412.

GEOFON Data Centre. (1993). *GEOFON seismic network*.Deutsches GeoForschungsZentrum GFZ. Other/seismic network. https://doi.org/10.14470/TR560404

Hafkenscheid, E., Buiter, S. J. H., Wortel, M. J. R., Spakman, W., & Bijwaard, H. (2001). Modelling the seismic velocity structure beneath Indonesia: A comparison with tomography. *Tectonophysics*, *333*(1–2), 35–46.

Hall, R. (2017). Southeast Asia: New views of the geology of the Malay archipelago. *Annual Review of Earth and Planetary Sciences*, *45*(1), 331–358.

Harris, R. (2006). Rise and fall of the Eastern Great Indonesian arc recorded by the assembly, dispersion and accretion of the Banda Terrane, Timor. *Gondwana Research*, *10*(3–4), 207–231.

Harris, R. (2011). The nature of the Banda arc–continent collision in the Timor-region. In D. Brown & P. D. Ryan (Eds.), *Arc–continent collision, frontiers in earth sciences* (pp. 163–211). Berlin: Springer. https://doi.org/10.1007/978-3-540-88558-0_7

Harris, C. W., Miller, M. S., Supendi, P., & Widiyantoro, S. (2020). Subducted lithospheric boundary tomographically imaged beneath arc-continent collision in eastern Indonesia. *Journal of Geophysical Research: Solid Earth*, *125*, e2019JB018854. https://doi.org/10.1029/2019JB018854

Herrmann, R. B. (2013). Computer programs in seismology: An evolving tool for instruction and research. *Seismological Research Letters*, *84*(6), 1081–1088.

Hilton, D. R., & Craig, H. (1989). A helium isotope transect along the Indonesian archipelago. *Nature*, *342*(6252), 906–908.

Hilton, D. R., Hoogewerff, J. A., Van Bergen, M. J., & Hammerschmidt, K. (1992). Mapping magma sources in the east Sunda–Banda arcs, Indonesia: Constraints from helium isotopes. *Geochimica et Cosmochimica Acta*, *56*(2), 851–859.

Keep, M., & Haig, D. W. (2010). Deformation and exhumation in Timor: Distinct stages of a young orogeny. *Tectonophysics*, *483*(1–2), 93–111.

Kennett, B. L., Engdahl, E. R., & Buland, R. (1995). Constraints on seismic velocities in the Earth from traveltimes. *Geophysical Journal International*, *122*(1), 108–124.

Ligorria, J. P., & Ammon, C. J. (1999). Iterative deconvolution and receiver-function estimation. *Bulletin of the Seismological Society of America*, *89*(5), 1395–1400.

Li, C., Yao, H., Fang, H., Huang, X., Wan, K., Zhang, H., & Wang, K. (2016). 3D near-surface shear-wave velocity structure from ambient-noise tomography and borehole data in the Hefei urban area, China. *Seismological Research Letters*, *87*(4), 882–892.

Luo, Y., Yang, Y., Xu, Y., Xu, H., Zhao, K., & Wang, K. (2015). On the limitations of inter-station distances in ambient noise tomography. *Geophysical Journal International*, *201*(2), 652–661. http://dx.doi.org/10.1093/gji/ggv043

Miller, M. S. (2014). Transitions in the Banda Arc-Australia continental collision, Dataset/Seismic Network, International Federation of Digital Seismograph Networks. https://doi.org/10.7914/SN/YS_2014

Miller, M. S., O'Driscoll, L. J., Roosmawati, N., Harris, C. W., Porritt, R. W., Widiyantoro, S., et al. (2016). Banda arc experiment—Transitions in the Banda arc–Australian continental collision. *Seismological Research Letters*, *87*(6), 1417–1423.

Petkovic, P., Collins, C. D. N., & Finlayson, D. M. (2000). A crustal transect between Precambrian Australia and the Timor Trough across the Vulcan Sub-basin. *Tectonophysics*, *329*(1–4), 23–38.

Phạm, T. S., & Tkalčić, H. (2017). On the feasibility and use of teleseismic P wave coda autocorrelation for mapping shallow seismic discontinuities. *Journal of Geophysical Research: Solid Earth*, *122*, 3776–3791. https://doi.org/10.1002/2017JB013975

Phạm, T. S., & Tkalčić, H. (2018). Antarctic ice properties revealed from teleseismic P wave coda autocorrelation. *Journal of Geophysical Research: Solid Earth*, *123*, 7896–7912. https://doi.org/10.1029/2018JB016115

Porritt, R. W., & Miller, M. S. (2018). Updates to FuncLab, a Matlab based GUI for handling receiver functions. *Computers & Geosciences*, *111*, 260–271.

Porritt, R. W., Miller, M. S., O'Driscoll, L. J., Harris, C. W., Roosmawati, N., & da Costa, L. T. (2016). Continent–arc collision in the Banda Arc imaged by ambient noise tomography. *Earth and Planetary Science Letters*, *449*, 246–258.

Pownall, J., Hall, R., & Watkinson, I. M. (2013). Extreme extension across Seram and Ambon, eastern Indonesia: Evidence for Banda slab rollback. *Solid Earth*, *4*(2), 277–314.

Shulgin, A., Kopp, H., Mueller, C., Lueschen, E., Planert, L., Engels, M., et al. (2009). Sunda–Banda arc transition: Incipient continent-island arc collision (northwest Australia). *Geophysical Research Letters*, *36*, L10304. https://doi.org/10.1029/2009GL037533

Siebert, L., & Simkin, T. (2002). *Volcanoes of the world: An illustrated catalog of Holocene volcanoes and their eruptions, global volcanism program, digital information series GVP-3*. Smithsonian Institution.

Spakman, W., & Hall, R. (2010). Surface deformation and slab–mantle interaction during Banda arc subduction rollback. *Nature Geoscience*, *3*(8), 562–566.

Supendi, P., Nugraha, A. D., Widiyantoro, S., Abdullah, C. I., Rawlinson, N., Cummins, P. R., et al. (2020). Fate of Forearc lithosphere at arc-continent collision zones: Evidence from local earthquake tomography of the Sunda–Banda Arc transition, Indonesia. *Geophysical Research Letters*, *47*, e2019GL086472. https://doi.org/10.1029/2019GL086472

Tate, G. W., McQuarrie, N., Tiranda, H., van Hinsbergen, D. J., Harris, R., Zachariasse, W. J., et al. (2017). Reconciling regional continuity with local variability in structure, uplift and exhumation of the Timor orogen. *Gondwana Research*, *49*, 364–386.

Tate, G. W., McQuarrie, N., van Hinsbergen, D. J., Bakker, R. R., Harris, R., & Jiang, H. (2015). Australia going down under: Quantifying continental subduction during arc–continent accretion in Timor-Leste. *Geosphere*, *11*(6), 1860–1883.

Tetreault, J. L., & Buiter, S. J. H. (2014). Future accreted terranes: A compilation of island arcs, oceanic plateaus, submarine ridges, seamounts, and continental fragments. *Solid Earth*, *5*(2), 1243–1275.

Widiyantoro, S., Pesicek, J. D., & Thurber, C. H. (2011). Complex structure of the lithospheric slab beneath the Banda arc, eastern Indonesia depicted by a seismic tomographic model. *Research in Geophysics*, *1*(1), e1.

Widiyantoro, S., & van der Hilst, R. (1996). Structure and evolution of lithospheric slab beneath the Sunda arc, Indonesia. *Science*, *271*(5255), 1566–1570.

Widiyantoro, S., & van der Hilst, R. (1997). Mantle structure beneath Indonesia inferred from high-resolution tomographic imaging. *Geophysical Journal International*, *130*(1), 167–182.

Zenonos, A., De Siena, L., Widiyantoro, S., & Rawlinson, N. (2019). P and S wave travel time tomography of the SE Asia–Australia collision zone. *Physics of the Earth and Planetary Interiors*, *293*, 106267.

Zenonos, A., De Siena, L., Widiyantoro, S., & Rawlinson, N. (2020). Direct inversion of S-P differential arrival times for Vp/Vs ratio in SE Asia. *Journal of Geophysical Research: Solid Earth*, *125*, e2019JB019152. https://doi.org/10.1029/2019JB019152

Zhang, P., Yao, H., Chen, L., Fang, L., Wu, Y., & Feng, J. (2019). Moho depth variations from receiver function imaging in the Northeastern North China craton and its tectonic implications. *Journal of Geophysical Research: Solid Earth*, *124*, 1852–1870. https://doi.org/10.1029/2018JB016122